AIP | Physics of Plasmas

Off-axis fishbone-like instability and excitation of resistive wall modes in JT-60U and DIII-D

M. Okabayashi, G. Matsunaga, J. S. deGrassie, W. W. Heidbrink, Y. In et al.

Citation: Phys. Plasmas **18**, 056112 (2011); doi: 10.1063/1.3575159
View online: http://dx.doi.org/10.1063/1.3575159
View Table of Contents: http://pop.aip.org/resource/1/PHPAEN/v18/i5
Published by the American Institute of Physics.

Related Articles

Collision frequency dependence of polarization current in neoclassical tearing modes
Phys. Plasmas 19, 032120 (2012)

Effects of beam temperature and density variation on the growth rate of a two-stream free electron laser
Phys. Plasmas 19, 032114 (2012)

The limits and challenges of error field correction for ITER
Phys. Plasmas 19, 056111 (2012)

Dynamic contraction of the positive column of a self-sustained glow discharge in molecular gas
Phys. Plasmas 19, 033512 (2012)

Wall-locking of kink modes in a line-tied screw pinch with a rotating wall
Phys. Plasmas 19, 056104 (2012)

Additional information on Phys. Plasmas

Journal Homepage: http://pop.aip.org/
Journal Information: http://pop.aip.org/about/about_the_journal
Top downloads: http://pop.aip.org/features/most_downloaded
Information for Authors: http://pop.aip.org/authors

ADVERTISEMENT

Downloaded 04 Apr 2012 to 129.16.35.96. Redistribution subject to AIP license or copyright; see http://pop.aip.org/about/rights_and_permissions

Off-axis fishbone-like instability and excitation of resistive wall modes in JT-60U and DIII-D[a)]

M. Okabayashi,[1,b)] G. Matsunaga,[2] J. S. deGrassie,[3] W. W. Heidbrink,[4] Y. In,[5] Y. Q. Liu,[6] H. Reimerdes,[7] W. M. Solomon,[1] E. J. Strait,[3] M. Takechi,[2] N. Asakura,[2] R. V. Budny,[1] G. L. Jackson,[3] J. M. Hanson,[7] R. J. La Haye,[3] M. J. Lanctot,[7] J. Manickam,[1] K. Shinohara,[2] and Y. B. Zhu[4]
[1]*Princeton Plasma Physics Laboratory, PO Box 451, Princeton, New Jersey 08543-0451, USA*
[2]*Japan Atomic Energy Agency, 801-1, Mukouyama, Naka, Ibaraki 311-0193, Japan*
[3]*General Atomics, PO Box 85608, San Diego, California 92186-5608, USA*
[4]*Department of Physics and Astronomy, University of California-Irvine, Irvine, California 92697, USA*
[5]*FAR-TECH, Inc., 3550 General Atomics Ct, San Diego, California 92121, USA*
[6]*Euratom/CCFE Fusion Association, Culham Science Centre, Abingdon, OX14 3DB, United Kingdom*
[7]*Department of Applied Physics and Applied Mathematics, Columbia University, New York, New York 10027-6900, USA*

(Received 16 December 2010; accepted 11 March 2011; published online 5 May 2011)

An energetic-particle (EP)-driven "off-axis-fishbone-like mode (OFM)" often triggers a resistive wall mode (RWM) in JT-60U and DIII-D devices, preventing long-duration high-β_N discharges. In these experiments, the EPs are energetic ions (70–85 keV) injected by neutral beams to produce high-pressure plasmas. EP-driven bursting events reduce the EP density and the plasma rotation simultaneously. These changes are significant in high-β_N low-rotation plasmas, where the RWM stability is predicted to be strongly influenced by the EP precession drift resonance and by the plasma rotation near the $q = 2$ surface (kinetic effects). Analysis of these effects on stability with a self-consistent perturbation to the mode structure using the MARS-K code showed that the impact of EP losses and rotation drop is sufficient to destabilize the RWM in low-rotation plasmas, when the plasma rotation normalized by Alfvén frequency is only a few tenths of a percent near the $q = 2$ surface. The OFM characteristics are very similar in JT-60U and DIII-D, including nonlinear mode evolution. The modes grow initially like a classical fishbone, and then the mode structure becomes strongly distorted. The dynamic response of the OFM to an applied $n = 1$ external field indicates that the mode retains its external kink character. These comparative studies suggest that an energetic particle-driven "off-axis-fishbone-like mode" is a new EP-driven branch of the external kink mode in wall-stabilized plasmas, analogous to the relationship of the classical fishbone branch to the internal kink mode. © *2011 American Institute of Physics*.
[doi:10.1063/1.3575159]

I. INTRODUCTION

The steady-state advanced tokamak (AT) regime is considered to be one of the most attractive candidates for fusion energy production. It has been predicted that high plasma pressure with high-β_N can sustain the plasma discharge by self-generating confining currents.[1] Here, the normalized beta, β_N, is a plasma stability index (Troyon parameter) defined as $\beta_T/(I_p/aB_T)$, where plasma beta β_T is represented as the ratio of volume-average plasma pressure p to the externally applied magnetic field pressure $B_T^2/2\mu_0$. B_T is the vacuum toroidal magnetic field, I_p is the plasma current, and a is the plasma minor radius at the midplane.

To achieve high plasma pressure, there exist several critical challenges in terms of MHD stability. The ideal external kink mode and its associated resistive wall mode (RWM) is one of them.[2,3] Once the plasma pressure exceeds a certain threshold, the ideal MHD no-wall limit, a low toroidal number $n = 1$ kink mode becomes unstable. If a perfectly conducting wall is located close to the plasma surface, the kink mode can be fully suppressed due to the eddy currents instantaneously induced on the wall when the mode is about to become unstable. In actual devices, finite wall resistivity allows the mode to grow more slowly. This mode is the RWM. Although the RWM growth rate is in the order of the inverse of the wall characteristic time $1/\tau_W$, the RWM growth must be suppressed, since the existence of a finite amplitude RWM induces various undesirable consequences such as magnetic island formation and plasma pressure collapse. The time constant τ_w is often estimated by $\mu_0 a\delta/\eta_w$, where a, δ, and η_w are the minor radius, the thickness of the resistive wall and the wall resistivity, respectively. The relation between the external kink and the RWM with finite wall resistivity is reviewed in Ref. 4.

RWM-stable plasma operation well above the no-wall limit was demonstrated by the JT-60U and DIII-D teams.[5–8] The stable window in plasma rotation was found to be broader than anticipated according to the criterion based on the original fluid MHD theory.[9] Significant stabilization by

[a)]Paper TI2 5, Bull. Am. Phys. Soc. **55**, 290 (2010).
[b)]Invited speaker.

 © 2011 American Institute of Physics

Downloaded 04 Apr 2012 to 129.16.35.96. Redistribution subject to AIP license or copyright; see http://pop.aip.org/about/rights_and_permissions

kinetic effects was predicted by Hu *et al.*,[10] taking into account the finite orbit effects of superthermal and thermal ions. In low-rotation plasmas, where the plasma rotation normalized by Alfvén frequency is only a few tenths of a percent near the $q = 2$ surface, RWM stabilization can be provided by the mode-particle resonance with the precession drift of trapped thermal ions and/or energetic particles (EPs) with RWM.[11–13] Thus, a large EP population has been considered as highly desirable. In the experiments described here, the energetic particles are high-energy ions (70–85 keV) injected by neutral beams to achieve high-pressure plasmas.

Although the high-β_N regime is achievable with heating by high power neutral beam injection (NBI), it is difficult to sustain high β discharges due to various types of MHD activity. During operation with high-β_N and the central safety factor $q(0)$ well above unity in JT-60U and DIII-D, the RWMs triggered by the EP-driven mode have been discovered to be one of the key challenges to discharge sustainment.[14,15] In JT-60U, frequent excitation of the EP-driven mode in the early phase of the discharge was a roadblock to reproducible achievement of long-pulse steady-state high-β_N discharges.[14,16,17] This EP-driven mode is named the "energetic-particle-driven wall mode (EWM)" in JT-60U emphasizing their observation in the wall-stabilized high-β_N plasmas, while in DIII-D the term "off-axis-fishbone-driven" RWM is used, since the mode has frequency chirping, similar to the classical fishbone even with $q(0)$ well above unity.[15] Herein, we use the terminology "off-axis-fishbone-like mode (OFM)" or simply "off-axis-fishbone" describing these bursting modes.

It has been observed at each EP-driven MHD event in DIII-D, that the plasma rotation was reduced simultaneously with the rapid decrease of neutron emission rate, based on the fast sampling of charge exchange recombination (CER) light measurement. The strong correlation between the rotation reduction and neutron emission drop implies that the rotation reduction is a consequence of a complex EP transport process.

There are two important aspects of the off-axis-fishbone-mode events: one is the off-axis-fishbone instability itself and the other is the RWM destabilization through bursting OFM events. From the view of the mode characteristics, a question arises as to whether the off-axis-fishbone-like mode is a new branch or not. A unique characteristic of OFM that occurs in the middle of the burst is a nonlinear mode distortion, which was observed both in the JT 60U and the DIII-D devices. The increase of EP losses during a burst coincided with the increase of mode distortion.

A schematic of the relationship between the RWM stability and EP-driven mode is illustrated in Fig. 1, using a paradigm of internal kink and classical fishbone.[18] For the low-frequency MHD mode with $f \leq f_{prec}$ (f_{prec} is the precession frequency of EPs), a finite EP population can provide MHD stabilization,[19,20] as was observed, for example, in the long sawtooth-free operation in JET.[21] On the other hand, with high power nearly perpendicular neutral beam injection experiments, large $m/n = 1/1$ bursting "classical fishbone" mode can be excited, reducing the EP population.[18] (m is the poloidal mode number and n is the toroidal mode number.)

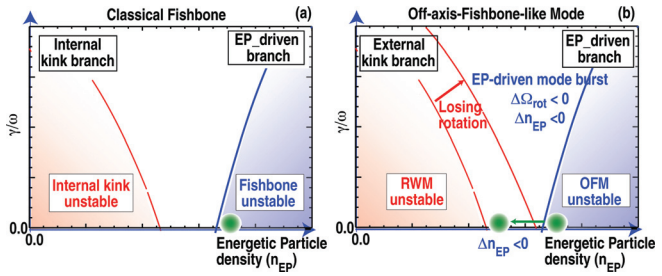

FIG. 1. (Color online) Schematics of EP-driven off-axis-fishbone-like mode and RWM stability showing growth rate vs energetic particle density. (a) The internal kink and classical fishbone and (b) the RWM branch and EP-driven branch. See text for explanation of the paradigm.

For the RWM, an external kink with resistive wall, its relation to the EP branch can be hypothesized as similar to that of the internal kink branch to the classical fishbone. This hypothesis implies that the EP-driven branch should behave as a classical fishbone, but with external kink character. With the EP losses due to OFM, the RWM becomes less stable. Furthermore, the rotation drop resulting from the EP transport losses can also decrease the RWM stability. Comparison of the MARS-K analysis[11] with experimental observation showed that these EP losses and rotation drop are sufficient to destabilize the RWM in low-rotation plasmas, where the plasma rotation normalized by Alfvén frequency is only a few tenths of a percent near the $q = 2$ surface.

We will discuss the analysis results with these two view points mentioned above, namely the OFM characteristics and the impact on the RWM stabilization. The commonality of the EP-driven modes observed in JT-60U and DIII-D is extremely helpful to clarify the fundamentals of EP-driven mode physics. Neutron reduction and rotation drop have not been clearly observed in the JT-60U experiments, so the discussion related on the neutron emission reduction and plasma rotation drop is based on the DIII-D results.

In Sec. II, we discuss the hardware and the experimental parameters of DIII-D and JT-60U. In Sec. III, the initial frequency and the neutron emission rate are presented in analogy to the "classical fishbone." The nonlinear distortion of EP driven mode is discussed in Sec. IV. The response to an applied $n = 1$ external field is presented in Sec. V. The MARS-K stability analysis is presented in Sec. VI. The discussions are presented in Sec. VII.

II. EXPERIMENTAL ARRANGEMENT

The experiments in JT-60U and DIII-D devices were carried out in a lower single null divertor configuration (Fig. 2). This configuration has been often used for high-β_N exploration in both devices.[14,15] For both devices, the q-profile was relatively flat near the magnetic axis with the central $q(0)$ well above unity.

In JT-60U, co-NBI ~12 MW and counter-NBI ~2 MW based on the positive ion sources were used for this experiment. In addition, the negative ion based tangential neutral beam injection of ~3 MW with ~350 keV beam energy was useful for heating without torque input. The JT-60U experiments explored high-β_N values close to the ideal wall limit,

Downloaded 04 Apr 2012 to 129.16.35.96. Redistribution subject to AIP license or copyright; see http://pop.aip.org/about/rights_and_permissions

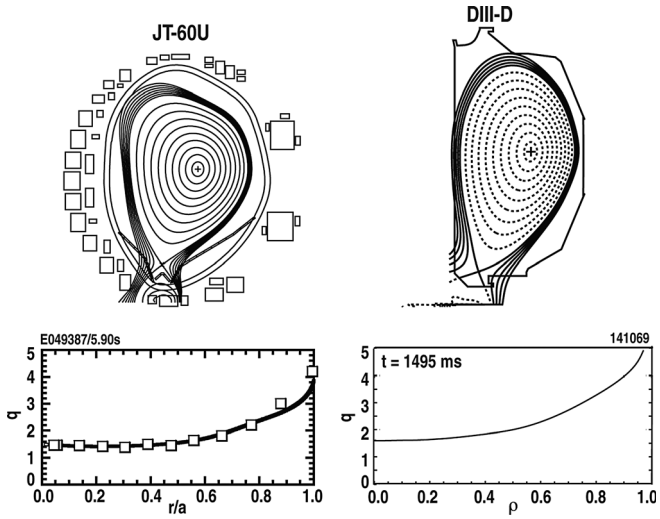

FIG. 2. JT-60U (left) and DIII-D (right) configurations and q-profiles.

$C_\beta = 0.8$, by lowering the toroidal field to 1.5 T with $I_p \sim 0.9$ MA. Here C_β is a measure of the gain in beta over the no-wall limit: $C_\beta = (\beta - \beta_{no-wall})/(\beta_{ideal-wall} - \beta_{no-wall})$, where the no-wall limit and ideal-wall limit are calculated with stability codes for the experimental condition. With this definition, $C_\beta = 0$ represents beta at the no-wall limit, and $C_\beta = 1$ represents beta at the ideal-wall limit. The stability limit was calculated using MARD2D[22] in JT-60U and GATO[23] and DCON[24] in DIII-D.

In DIII-D, co-NBI $\leq$ 15 MW and counter-NBI $\leq$ 5 MW were used for this experiment. Most of the discharges from DIII-D discussed in this paper were carried out by applying electron cyclotron current drive (ECCD) power of 3 MW for preemptive neoclassical tearing mode (NTM) avoidance. This constrained the toroidal field to 1.6–1.7 T with $I_p \sim 1$ MA for producing $q = 2$ around $\rho = 0.6$. In the present experiments, the C_β was $\sim$0.4. This fixed toroidal field also limited the radial coverage of electron cyclotron emission (ECE) diagnostics. The plasma parameters for JT-60U and DIII-D are listed in Table I. The estimate of the wall time constant τ_w for the JT-60U using the skin time $\mu_0 a\delta/\eta_w$ is $\sim$10 ms.[6] The decay time for the DIII-D estimated using the VALEN code[25] is 2–5 ms for the slowest nonaxisymmetric eigenvalue of the DIII-D vacuum vessel structure.

TABLE I. Typical JT-60U and DIII-D plasma parameters where EP modes were observed. (For DIII-D, the parameters used for the MARS-K analysis.) The estimate for the JT-60U was with $\tau_w = \mu_0 d\delta/\eta_w$(Ref. 6). The decay time for the DIII-D was estimated using VALEN code (Ref. 25).

	JT-60U	DIII-D
β_N: no-wall	2.4	2.1
β_N: ideal-wall	3.2	2.6
β_N: (exp)	3.0	2.3
C_β	0.8	0.4
B_0(T)	1.5–1.7	1.7
I_p(MA)	0.9	1.1
R_0(m)	3.6	1.7
$q(0)$	1.5	1.6
q_{95}	$\sim$3.3	4.6
$\Omega_{rot}(0)/\Omega_A$	$<$1%	4%
Ω_{rot}(at $q = 2$)/Ω_A	$\sim$0.2%	0.6%
n_{EP}/n_e(at $q = 2$)	10%	$\sim$5%
P_{EP}/P_e(at $q = 2$)	60%	$\sim$35%
n_e (m^{-3})	2×10^{19}	3×10^{19}
τ_w (ms)	$\sim$10	2–5

In DIII-D, the RWM feedback system is also used to examine the mode character by the response to the applied external field. The feedback hardware used was a standard feedback hardware arrangement.[26] The two arrays of six feedback I-coils are located inside the vacuum vessel above and below the midplane. The connection of the upper/lower coils was optimized for producing the $m/n = 3/1$ mode pattern. The feedback $n = 1$ signal was prepared using the poloidal magnetic field probes located at the midplane. More details about the hardware are found in Ref. 26. The experimental results reported here were carried out without feedback applied except for those in Sec. V.

III. OFF-AXIS FISHBONE AND RWM ONSET

Typical example of $n = 1$ RWM excitation in the JT-60U and the DIII-D are shown in Fig. 3. As shown in Figs. 3(a) and 3(e), in both devices, series of bursting modes were observed by the δT_e-ECE measurement, finally leading to

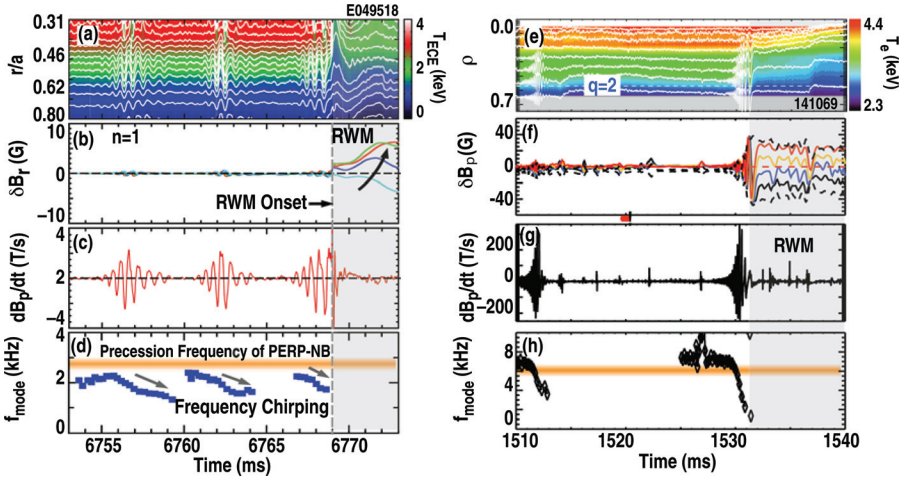

FIG. 3. (Color online) The EP-driven mode and the excitation of RWM of JT-60U (left) and DIII-D (right). The figures of (a)–(d) are for the JT-60U, #E049518, while those of (e)–(h) are for DIII-D discharge, #141069. For JT-60U, (a) the δT_e-ECE fluctuation is shown over the T_e-ECE contour, (b) the $n = 1$ component of integrated saddle loop signals at four toroidal locations, (c) dBp/dt signal and (d) the instantaneous mode frequency of magnetic dBp/dt probe signal. For DIII-D, (e) the δT_e-ECE fluctuation is shown over the T_e-ECE contour, (f) the $n = 1$ component of integrated poloidal magnetic probe signals at four toroidal locations, (g) dBp/dt signal, (h) the instantaneous mode frequency of magnetic dBp/dt probe signal.

Downloaded 04 Apr 2012 to 129.16.35.96. Redistribution subject to AIP license or copyright; see http://pop.aip.org/about/rights_and_permissions

the onset of a RWM. The δT_e-ECE signals [Figs. 3(a) and 3(e)] show that the mode excitation took place with the peak located around $r/a = 0.5$–0.6 in JT-60U (r/a is defined as volume-averaged radius) and $\rho = 0.5$–0.6 in DIII-D (ρ is defined with normalized toroidal flux). These bursting modes observed by magnetic probes as shown in Figs. 3(c) and 3(g), in JT-60U, the repetition rate of modes is rather fast (every 4–5 ms). In DIII-D, the repetition period was longer ~20 ms. The difference of the repetition rate may be attributable to the higher fast-ion pressure in JT-60U compared with in DIII-D.

The initial mode frequencies of bursting modes were ~3 kHz in the JT-60U and ~7 kHz in the DIII-D, respectively [Figs. 3(d) and 3(h)]. These are close to the precession frequencies of trapped EPs in both devices. The precession frequency of 3 kHz (JT-60U) and 6 kHz (DIII-D) were calculated with the orbit-following-Monte–Carlo code.[27] The frequency chirped down by Δf ~1 kHz (JT-60U) and ~5 kHz (DIII-D). After the chirping, the final frequency became comparable to the plasma rotation frequency of ~1 kHz near $q = 2$ before the RWM became unstable. The relation to the plasma rotation profile was discussed in detail in Refs. 14 and 15. The RWM growth is shown in Figs. 3(b) and 3(f). In JT-60U, the $n = 1$ growth was monitored with $n = 1$ component of saddle magnetic loops toroidally distributed inside the vacuum vessel. As shown with four $n = 1$ sensor signals, the $n = 1$ RWM grew rapidly near the end of EP-driven mode, and then grew in a slowly rotating manner (a couple of hundred hertz) with the $n = 1$ amplitude reaching $\delta B_r = 5$ G. In DIII-D, the $n = 1$ RWM was monitored using poloidal magnetic probes toroidally distributed at eight different locations. As shown in Fig. 3(f), the bursting mode in DIII-D developed into a $n = 1$ RWM of $\delta B_p = 20$–30 G without much subsequent increase in amplitude, in contrast to JT-60U. In both devices, the onset of RWM caused mini-collapse in pressure, as seen in T_e contour plots shown in Figs. 3(a) and 3(e). In both devices, the mode amplitude was maximum around $q = 2$ (details in Sec. IV). The growth time in JT-60U was 1–2 ms with 200–300 Hz oscillatory behavior. In DIII-D, however, the initial growth may be marginally unstable judging from quasistationary behavior before it became nonlinearly leading to the mini-collapse. The difference in these growth rates may be related to the plasma condition. Further systematic scans are needed to compare the details of growth time characteristics in both devices.

The onset of RWM-driven by the EP mode takes place near the operational limit previously observed. In Fig. 4, RWM onsets previously reported in Ref. 5 are shown with time trajectories in the domain of normalized C_β and normalized rotation $\Omega\tau_A$. The trajectories obtained in the previous experiments are shown with gray color and the onset of RWM is marked with square symbol. It should be noted that in this marginal domain in the plasma rotation and C_β diagram, not only the RWM, but also the NTM caused beta collapse in the DIII-D as reported in Ref. 15. This coincidence of the various stability limit domains is similar to the behavior in JT-60U,[14] which showed the onset of EP-driven RWM and other MHD, including the NTM that took place in a very similar parameter range of the plasma rotation and C_β diagram.

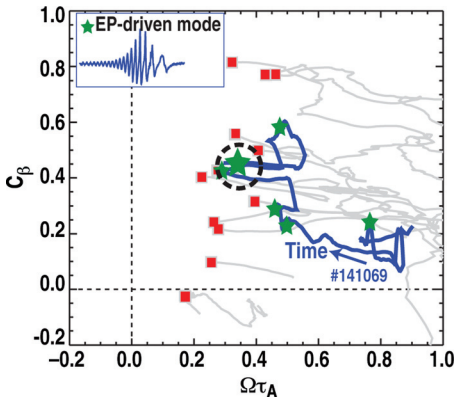

FIG. 4. (Color online) A trajectory of the DIII-D plasma shown in Fig 3. (#141069) in the domain of normalized β_N limit C_β vs. normalized plasma rotation in comparison with operational limit previously reported in Ref. 8. Trajectories with "gray color" are several discharges terminated by a RWM and the onset of RWM is marked with square box (from Fig. 4 in Ref. 8). Marked with a "star" on the solid line are the OFM events in the plasma shown in Fig. 3. The last event took place with $C_\beta \sim 0.4$ and normalized rotation = 0.2%–0.3% (marked with dashed circle) (DIII-D).

A typical trajectory of EP-driven mode and the following onset of RWM (#141069) is shown with blue curve. Above $C_\beta \sim 0.2$, EP-driven modes were excited (marked with "star") when the plasma rotation was reduced by lowering the NBI injected torque. The last event took place with $C_\beta \sim 0.4$ and normalized rotation ~0.2%–0.3% (marked with dashed circle). The fact that the RWM onset in the presence of the EP-driven mode belongs to the domain previously documented implies that the characteristics of EP-driven mode at low rotation and its RWM onset will provide the fundamental information of RWM onset mechanism.

A. Initial frequency

The EP precession role for the bursting MHD is clearly observable in the initial mode frequency dependence on the plasma rotation. Figure 5 shows a plot of the observed initial frequencies of DIII-D and JT-60U vs. the plasma rotation

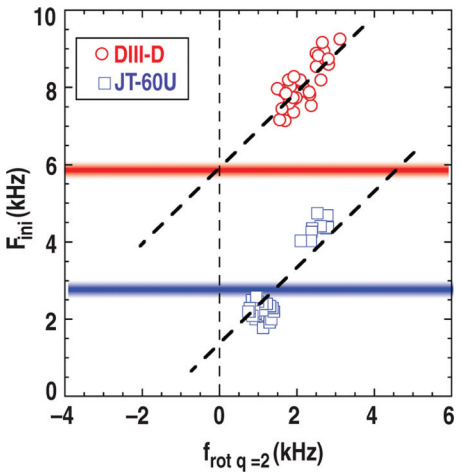

FIG. 5. (Color online) Initial frequency of the OFM vs. plasma rotation frequency, f_{rot} around $q = 2$ surface. The horizontal bar indicates the precession drift frequency for JT-60U and DIII D calculated by orbit-following-Monte–Carlo code (Ref. 27)

Downloaded 04 Apr 2012 to 129.16.35.96. Redistribution subject to AIP license or copyright; see http://pop.aip.org/about/rights_and_permissions

around the $q = 2$ surface before the mode onset. The range of rotation in each device where this mode was observed was rather narrow. However, the dependence in both devices shows a clear off-set linear relationship between the initial frequency f_{ini} and the plasma rotation frequency f_{rot} at $q = 2$,

$$f_{ini} = f_{prec} + f_{rot}. \quad (1)$$

The carbon impurity rotation velocity measured by the charge exchange recombination spectroscopy was used to measure the plasma rotation frequency f_{rot}. The results showed that the initial frequency was Doppler-shifted by the plasma rotation. The precession frequency f_{prec} of trapped EPs is ~3 kHz with 85 keV NBI ions in JT-60U and ~6 kHz with 70 keV NBI ions in DIII-D according to the orbit-following-Monte–Carlo code. This indicates that these modes were driven by the trapped EPs resonance with the injected ions of the initial beam energy. These observations are consistent with a hypothesis that the EP-driven modes are excited in a mechanism similar to the one in the classical fishbone in the initial stage of mode growth.[28] However, JT-60U results (dotted line) show the off-set somewhat different from the estimated precession frequency. One possibility is that the precession frequency of EPs is not sharp due to its slowing-down process. Thus, driving source of EPs broadly exists in the kilohertz-range. Another possibility is that the mode frequency is influenced by the stable external kink-ballooning branch rather than by the EP- precession frequency. An interpretation of the dependence of the initial frequency and plasma rotation needs further experimental studies.

B. Energetic ion loss

In the early stage of bursting, another comparison of the off-axis fishbone-like mode to the classical fishbone is made by observing the neutron emission dependence on the mode amplitude. The neutron emission rate provides the time evolution of EP density. According to TRANSP analysis of discharges in DIII-D, 73% of neutron production is by beam-plasma, 20% by thermonuclear, and 7% by beam-beam. Based on these analyses, we conclude that the ratio of the incremental change of EP density to the incremental change of neutron emission rate is near unity. Thus, the time evolution of the neutron emission can be interpreted as the time evolution of EP density. Figure 6 shows the maximum value of the neutron loss rate evaluated by the instantaneous rate of change of the neutron emission, $-dI_{neu}/dt/I_{neu}$, vs. the peak magnetic probe amplitude in DIII-D. For this analysis, the periodic behavior of the neutron emission was eliminated by smoothing. The rate of change in the neutron emission is strongly correlated with the peak magnetic probe amplitude. The curves shown here are three possible fits: quadratic, off-set linear, and linear. Approximately, these scalings correspond to: diffusion, threshold of some nonlinear process (perhaps associated with island overlap), and pure convective transport, respectively. These possible processes were discussed in detail in Ref. 29. The classic fishbone agreed well with linear dependence as described by "mode-particle pumping."[30] The data fit off-set linear (12% error) and quadratic (16% error) better than linear scaling, but the scatter is too large to draw a definitive conclusion.

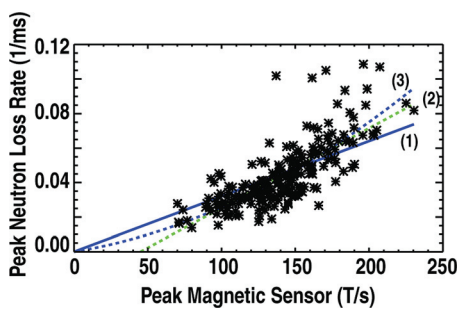

FIG. 6. (Color online) Peak rate of change in neutron emission $-dI_{neu}/dt/I_{neu}$ (1/ms) vs. peak magnetic dBp/dt probe amplitude in DIII-D. The curves shown here are three possible fits: (1) linear, (2) off-set linear, and (3) quadratic.

C. Rotation reduction with OFM

Figure 7 shows the reduction in toroidal rotation frequency at the fishbone burst in DIII-D. Here, the average was taken for eight reproducible bursting modes with similar parameters and CER data acquired with sampling time interval of 0.5 ms. Figures 7(a) and 7(b) show the instantaneous change in neutron emission $-dI_{neu}/dt/I_{neu}$ and the toroidal velocity at $q = 2$. The radial profile of incremental rotation reduction around $q = 2$ surface is given in Fig. 7(c), where the error bars are from the standard deviations of the eight off-axis-fishbones. The decrease of 10 km/s in the outer

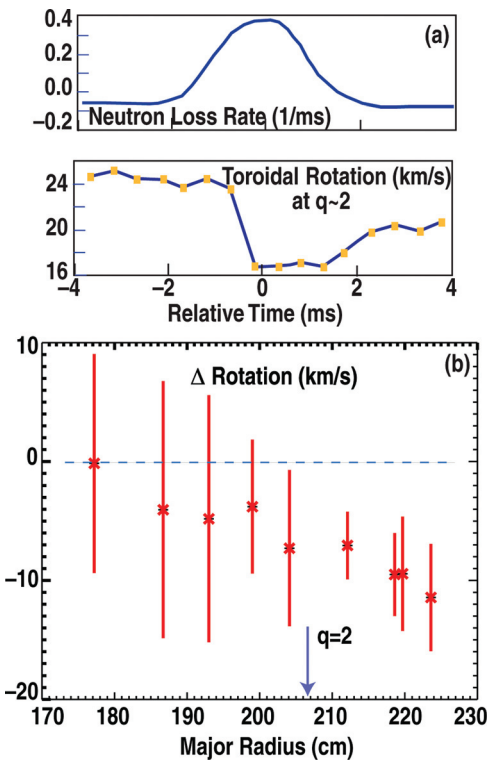

FIG. 7. (Color online) Relationship of the rotation reduction with rate of change in neutron emission, based on eight reproducible shots in DIII-D. (a) The instantaneous rate of change in neutron emission, $-dI_{neu}/dt/I_{neu}$. (b) The toroidal plasma rotation around $q = 2$, and (c) the reduction of plasma rotation vs. major radius.

Downloaded 04 Apr 2012 to 129.16.35.96. Redistribution subject to AIP license or copyright; see http://pop.aip.org/about/rights_and_permissions

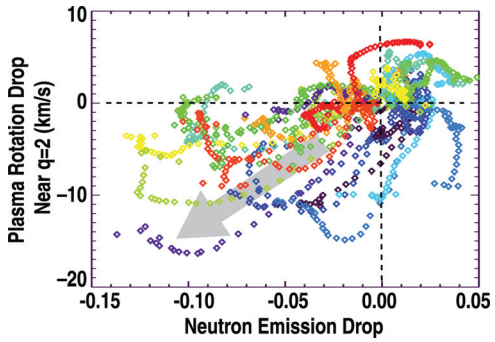

FIG. 8. (Color) Time evolution of rotation near $q = 2$ vs. time evolution of neutron emission after bursting events took place. This includes over 40 OFM events during 500 ms of two shots (#141086, #141092, 1500–2000 ms) in DIII-D discharges.

radius is attributable to the torque impulse associated with nonambipolar transport of the fast-ions at the fishbone burst as discussed below. If we interpret this change as being caused by a change in E_r, then the precession frequency should drop by ~0.7 kHz. In experiments, the observed mode frequency drops 2.5 kHz. Thus, the change in E_r can account for a portion of the frequency chirp but not the entire chirp. Assuming that the mode is an EP-driven mode, the additional frequency sweep is probably caused by preferential loss of high-energy fast-ions that have large values of f_{prec}.

The incremental change of plasma rotation $\Delta V_\phi(t)$ from the onset of the burst is correlated with the incremental change of neutron emission rate from the onset of the burst, $\Delta I_{neu}(t)$ as shown in Fig. 8. The parametric dependence in the domain of negative quadrant shows the rotation drops in a monotonical manner with the decrease of neutron emission rate.

These time traces are over 0.5 s of two shots, including more than 40 events of EP-driven modes. In the present experiment, the NBI power was modulated to maintain a nearly constant normalized beta of around 2.4. The power modulation was ±2–3 MW over the total injected power ~12 MW by switching on/off several NB sources with a switching interval of 10–15 ms, compensating the stored energy loss presumably due to the OFM. However, the NBI power was modulated without precise correlation to the timing of OFM onset, causing the large scatter in the parametric dependence in Fig. 8.

In these shots, the initial rotation before the EP-driven mode event was kept high enough to avoid the RWM onset. Occasionally, the rotation drop reached 15 km/s, but typically the value was ~10 km/s with 7%–10% neutron drop. The 10% neutron drop corresponded to ~10% of EP losses based on the TRANSP analysis as discussed before.

These observed correlations suggest EP losses during fast-ion loss are responsible for the rotation reduction. One possible mechanism is nonambipolar radial electric field buildup.

The toroidal angular momentum balance can be given by Ref. 31,

$$M_i n_i d\langle R_0 V\rangle_\phi \Big/ dt = \langle J_i \nabla\psi\rangle, \tag{2}$$

where M_i is the ion mass, n_i is the ion density, R_0 is the major radius, J_i is the ion polarization current responding to the EP loss, and ψ is the poloidal flux function. Since the EP losses take place much faster than the scattering time of the perpendicular energetic ion and the average slowing-down time of the energetic ion, it is possible to neglect the momentum viscosity properties in Eq. (2), allowing to estimate the relationship between the momentum input and the change of radial electric field.

The bulk ion polarization current responds to the EP loss by maintaining the total radial current nearly zero.

$$\langle J_i \cdot \nabla\psi\rangle = -\langle J_{EP} \cdot \nabla\psi\rangle, \tag{3}$$

$$\langle J_{EP} \cdot \nabla\psi\rangle = e n_{EP} V_{EP} R B_p, \tag{4}$$

where the momentum drop is approximated using the energetic particle density n_{EP} and the energetic particle radial drift velocity V_{EP}.

By integrating Eq. (2) over the bursting time period, the rotation drop ΔV_ϕ can be expressed by

$$r_{EP,shift} = \int dt V_{EP}, \tag{5}$$

$$\Delta V_\phi = -(\Delta n_{EP}/n_i)(eB_p/M_i) r_{EP,shift}, \tag{6}$$

where $r_{EP,shift}$ is the effective radial shift of the EP which produces the radial EP current and Δn_{EP} is the drop of EP density before and after the OFM event. Here, in the polarization current buildup process, it is assumed that the electrons are tied to the magnetic surface.

For the parameter set of experimental condition, $n_{EP}/n_i = 5\%$, $\Delta n_{EP}/n_{EP} = 10\%$, the required size of the EP shift $r_{EP,shift}$ is ~15 cm. This size is comparable to the size of the radial mode structure as discussed in Sec. IV B.

IV. MODE DISTORTION

The magnetic probe signals in both JT-60U and DIII-D show two distinctive features compared with the classical fishbone. One is the nonlinear mode distortion around the mode maximum amplitude and the other is the mode decay time. Typical examples are shown in Fig. 9. On the midplane magnetic probe signals [Figs. 9(a) and 9(d)], the mode amplitude asymmetry became visible after the mode reached maximum amplitude. On the off-midplane probes the distortion was clearly observable in both devices as shown in Figs. 9(b) and 9(e) and with the expanded time scale in Figs. 9(c) and 9(f). The poloidal location of off-midplane probes are chosen near the poloidal angle $\theta = \pm 60°$ for detecting $m = 3$ component for both devices.

Before the mode distortion occurs, the waveform of the upper/lower magnetic probe is in phase, consistent with a shift of one wavelength as expected for $m = 3$ component. (However, it has to be noted that since the mode amplitude at the high field side is smaller than that at the low field side, the poloidal mode structure is not a simple $m = 3$ structure. The m-number should be interpreted as "local m number" at

Downloaded 04 Apr 2012 to 129.16.35.96. Redistribution subject to AIP license or copyright; see http://pop.aip.org/about/rights_and_permissions

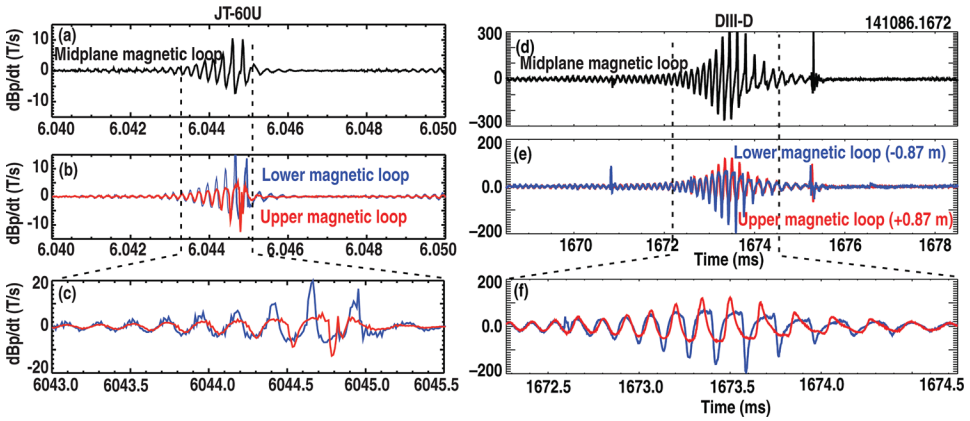

FIG. 9. (Color) Mode distortion observed on upper/lower magnetic probe in JT-60U (E049825) (left) and DIII-D shot #141086(right). (a) and (d) Midplane magnetic probe, (b) and (e) upper/lower magnetic probe, and (c) and (f) upper/lower magnetic probe details with 2.5 ms time coverage. Magnetic loops are located at $\theta \approx \pm 60°$ both in JT-60U and DIII-D. (More precisely, in JT-60U, the upper probe is located at $\theta = +68°$ and lower probe is at $\theta = -53.21°$. In DIII D, the off-midplane upper/lower probes are located at located at $\theta = \pm 57°$.)

the outboard side.) Once the mode amplitude becomes larger, the distortion grows much faster than the fundamental $m = 3$ structure in both devices. After the mode distortion decays away, the mode recovers its dominantly $m = 3$ component character in both devices. It is to be noted that the distortion is not the same in the upper and lower magnetic signals. Details will be discussed later in this section.

The mode decay time seems complex as seen in Figs. 9(a) and 9(d). The decay rate in both JT-60U and DIII-D is rather short compared with the classical fishbone where the decay time is much longer than the initial growth time. Mode distortion could occur due to the existence of a nonaxisymmetric magnetic field (error magnetic field). This possibility is ruled out since the distorted mode rotates uniformly in the toroidal direction; thus, it is not likely that the distortion is due to a local uncorrected error field. We discuss next the correlation of EP loss to the mode distortion, the distortion radial and poloidal structure.

A. Correlation of EP loss and mode distortion

A unique feature of the OFM in contrast to the classical fishbone is nonlinear mode distortion as observed in both DIII-D and JT-60U. In DIII-D, the increase of EP loss rate observed by the beam-ion loss detector (BILD)[32] coincided with the increase of the mode distortion, as shown in Fig. 10. The magnitude of distortion is shown by Fourier decomposing the magnetic fluctuation in one cycle, assuming that the mode rotates toroidally as a rigid structure and the distortion takes place slowly compared with the toroidal rotation. The harmonics can be interpreted as the contribution of higher toroidal-n components. When the mode distortion is smaller, the mode is dominantly composed of the $n = 1$ fundamental. The amplitude of mode numbers $n = 3$ and 4 increased just before the maximum of fast-ion loss occurred.

In JT-60U, synchronized signals with OFM were observed by measurements in the scrape-off layer (SOL). Figure 11 shows floating potential measured by Langmuir probes on divertor targets at the high field side in the divertor chamber and the magnetic fluctuation signals at upper and lower location of the outer midplane monitoring the mode distortion. (The details of the poloidal magnetic probe signals are given in the Sec. IV C.) Usually, floating potential at the divertor target detects the global SOL behavior since the potential is constant along magnetic field lines. Positive spikes up to ~100 V were observed, which coincided with higher mode distortion. We interpret the SOL potential increase as increased positive charge due to enhanced ion transport to SOL. Although this is not direct measurement of EP, the positive sharp spikes are consistent with EP losses to SOL region.

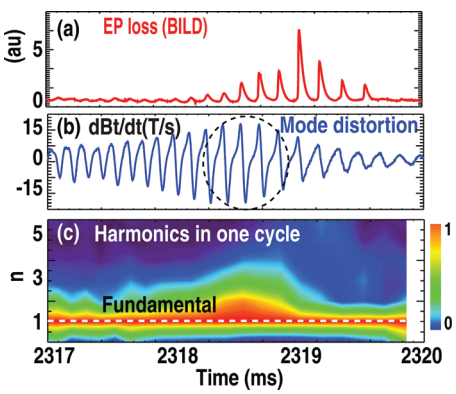

FIG. 10. (Color online) The increase in the EP loss coincides with the increase of mode distortion in DIII-D (#141089). (a) Beam-ion loss detector, (b) the toroidal magnetic probe signal, and (c) the harmonic content in one cycle period. The harmonics correspond to the toroidal n number. The color bar (0,1) represents the harmonics amplitude of magnetic probe signal normalized by the maximum value at $t = 2318.8$ ms.

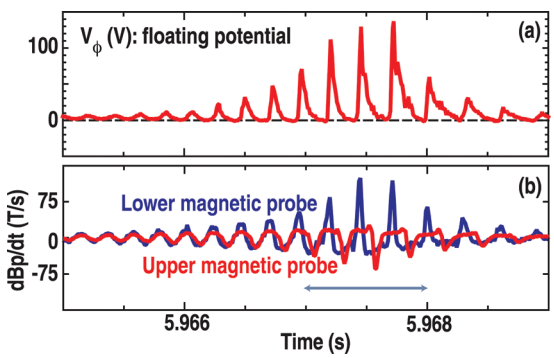

FIG. 11. (Color online) Time evolution of the floating potential and magnetic probe signals during OFM in JT-60U (E049825). (a) Floating potential measured by Langmuir probes on divertor targets at HFS and (b) magnetic probe signals at upper and lower location of the outer midplane. The upper probe is located at $\theta = +68.0°$ and lower probe is at $\theta = -53.21°$.

Downloaded 04 Apr 2012 to 129.16.35.96. Redistribution subject to AIP license or copyright; see http://pop.aip.org/about/rights_and_permissions

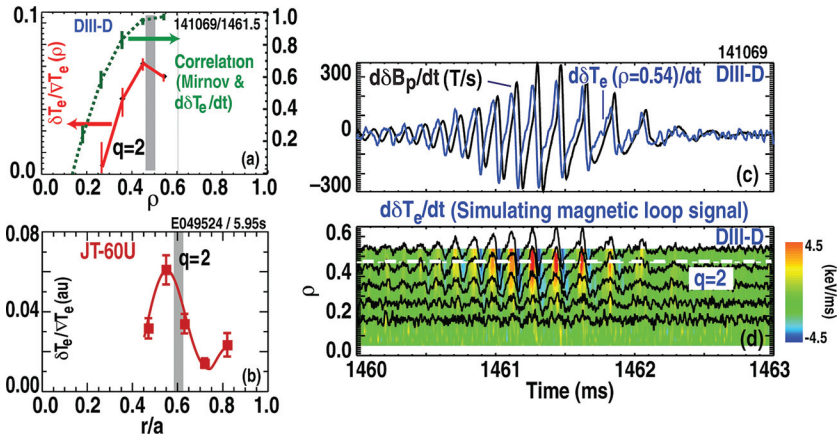

FIG. 12. (Color) Mode radial structure. (a) DIII-D (#141069) mode radial profile δT_e-ECE/∇T_e and the correlation between the magnetic probe and $d\delta T_e/dt$, (b) JT-60U (#E049524) mode radial profile $dT_e/\nabla T_e$, (c) DIII-D comparison of dBp/dt magnetic probe signal with the time derivative of δT_e-ECE at $\rho = 0.54$ near $q = 2$, and (d) DIII-D $d\delta T_e/dt$ signals (black lines) and contours of the time derivative of δT_e-ECE vs. ρ.

These results in both DIII-D and JT-60U indicate that the increase of mode distortion took place simultaneously with an increase of the EP loss.

B. Radial structure of mode distortion

The mode structure is located with a maximum peak around $q = 2$ both in JT-60U and DIII-D as shown in Fig. 12. The mode profile $\delta T_e/\nabla T_e$ in DIII-D [Fig. 12(a)] seems to be a little wider, compared to the structure in JT-60U [Fig. 12(b)]. (The DIII-D radial coverage of ECE [Fig. 12(a)] is limited due to the choice of the toroidal field strength adjusted for NTM preemptive suppression). The radial extension of the mode distortion is shown by taking the time derivative of ECE electron temperature and then by comparing the $\dot{B}$ probe (dB_p/dt) signal as shown in Fig. 12(c). The ECE signal with the time derivative near the $q = 2$ matches well with the magnetic signals, by taking into account the relative toroidal location difference of 13° between two systems. The evolution of the radial profile distortion is shown by the contour of time derivative of δT_e-ECE signal in Fig. 12(d). The maximum correlation between magnetic probe signal and the time derivative of δT_e-ECE was calculated at $t = 1461.3$ ms by allowing the phase shift over one cycle time period, since the two systems are slightly separated as discussed previously. The maximum correlation is above 0.9 near $q = 2$ and remains high like ~0.8 [Fig. 12(a)], with the half-width of the maximum correlation, $\Delta\rho \sim 0.25$ (corresponding to 0.15–0.2 m) in DIII-D. The half-width in JT-60U is $\Delta\rho \sim 0.15$. This suggests that the mode structure including the mode distortion behaves like one rigid body. In this analysis, the phase shift in the radial direction was not determined, since we allowed the phase shift over one cycle time period, and due to the toroidal angle separation between two systems.

C. Poloidal structure of mode distortion

In the beginning of this section, we discussed the upper/lower magnetic probe asymmetry. Here, we discuss the mode distortion over about one poloidal wavelength using poloidal magnetic probe array. In DIII-D, about a dozen of magnetic probe sensors are located with nearly-equal poloidal separation on the outboard side, covering about one and half of wavelength of $m = 3$ component as shown in Fig. 13. The $m = 3$ component, before the mode distortion started, provides the geometrical relationship of the poloidal magnetic probe arrays signal to magnetic pitch angle of $q = 3$. Once the projection of the $m = 3$ angle to the poloidal array signal is given as shown in Fig. 13(a), we can determine the mode distortion peaking character.

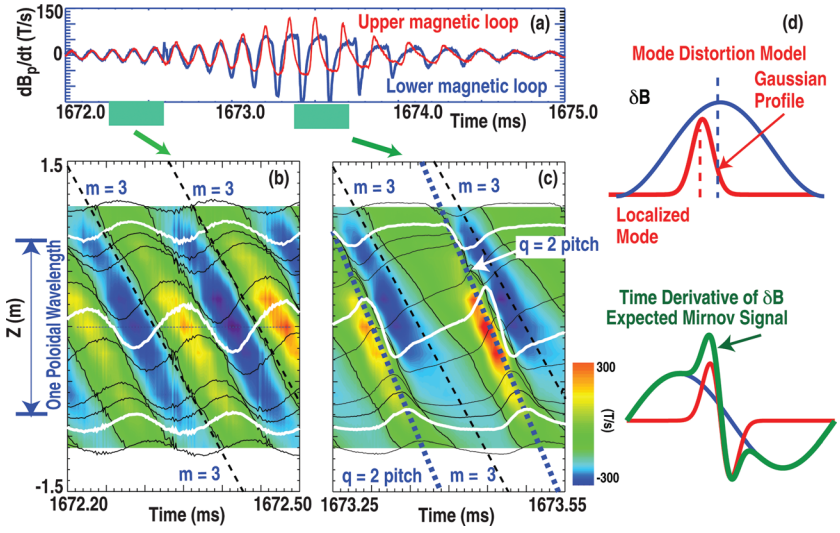

FIG. 13. (Color) Poloidal mode structure contour covering over one poloidal wavelength of $m = 3$ component in DIII-D (#141086). (a) Upper/lower magnetic probe signals and (b) poloidal structure before the mode distortion. On the contour of dBp/dt signal magnitude, the magnetic probe signals are superimposed. The dashed line is for $m = 3$ pitch angle and the thicker dashed line is for $q = 2$ pitch angle, (c) poloidal structure during the mode distortion, (d) the distortion model with Gaussian profile (red curve) and $m = 3$ component with sinusoidal blue curve. The summation of derivative curves (green curve) was compared with magnetic dBp/dt probe signals at various poloidal location.

Downloaded 04 Apr 2012 to 129.16.35.96. Redistribution subject to AIP license or copyright; see http://pop.aip.org/about/rights_and_permissions

By assuming the mode remains rigid while it rotates toroidally, the dominantly $m = 3$ oscillation signal and mode distortion are modeled with a sinusoidal oscillation, δB_{mi} [Fig. 13(d)],

$$\delta B_{\mathrm{m=3,i}} = A_{\mathrm{m=3,i}} \sin[\phi(t) - \phi_{\mathrm{m=3,o}}(\theta_{\mathrm{i}})], \tag{7}$$

and a localized pulse representing the mode distortion δB_{di} with a Gaussian profile,

$$\delta B_{\mathrm{di}} = A_{\mathrm{di}} \exp\{-[\phi(t) - \phi_{\mathrm{d}}(\theta_{\mathrm{i}})]/\Delta\phi_{\mathrm{d}}(\theta_{\mathrm{i}})\}^2. \tag{8}$$

The total waveform is $\delta Bp_{\mathrm{i}} = \delta B_{\mathrm{m=3,i}} + \delta B_{\mathrm{di}}$, where θ is the poloidal angle, the subscript i is for the poloidal array identification index, $\phi_{\mathrm{d}}(\theta_{\mathrm{i}})$ is the phase of the center of the localized pulse at poloidal angle $\theta = \theta_{\mathrm{i}}$, and $\Delta\phi_{\mathrm{d}}(\theta_{\mathrm{i}})$ is the width of the pulse at poloidal angle $\theta = \theta_{\mathrm{i}}$. With the assumption of the rigid body rotation, the time is translated to the toroidal phase ϕ, $t = \tau_{\mathrm{m}}\phi/(2\pi)$, where τ_{m} is one oscillation time period. The result shows that the phase of the center of the localized pulse $\phi_{\mathrm{d}}(\theta_{\mathrm{i}})$ follows the $q = 2$ pitch and the width of the pulse $\Delta\phi_{\mathrm{i}}$ at midplane $\sim 30^{\circ}$ from the maximum of $m = 3$ component. The result that the phase of the center of the mode distortion $\phi_{\mathrm{d}}(\theta_{\mathrm{i}})$ follows $q = 2$ pitch implies some resonance should take place around $q = 2$ area.

In the JT-60U, a similar poloidal mode structure was observed. However, limited locations of poloidal probes made it impossible to distinguish the $m = 2$, 3 components in a quantitative manner.

D. Spatial structure of EP loss

Comparison of the EP diagnostic signals with a magnetic probe provides the phase of the EP losses during an OFM event. Several EP diagnostics detectors have been installed at various toroidal and poloidal locations in DIII-D. These EP diagnostics include ion cyclotron emission (ICE), beam-ion loss detector (BILD), neutral particle analyzers (NPA), Langmuir probe ion saturation current (ISAT), fast-ion D-alpha light (FDIA), and a fast-ion loss detector (FILD). The details of some of these diagnostics are discussed in Refs. 32–35.

All of these loss diagnostics observe coherent bursts of fast-ion loss that are synchronized with the magnetic oscillations. For every diagnostic, the phase of the burst relative to the magnetic dBp/dt probe signal is virtually identical on every cycle. For most of the loss diagnostics, the largest bursts occur after the mode has reached its maximum amplitude, as illustrated in Fig. 10(a) for the beam-ion loss detector.

Toroidally separated loss diagnostics that measure the same physical quantity (e.g., two toroidally separated FIDA detectors) observe an $n = 1$ structure to the losses. The phase difference between different diagnostics requires more complicated geometrical consideration as well as individual diagnostic subtleties. Further discussion of the loss measurements appears in Ref. 36.

V. RESPONSE TO APPLIED $n = 1$ EXTERNAL FIELD

A question arises as to whether the off-axis-fishbone-like mode has the characteristics of external kink. One approach to answer this issue is to examine whether the mode can respond to an applied $n = 1$ external field. If the $n = 1$ external field interacts with the mode, it suggests that the mode has the external kink character. Here, the RWM feedback system is used for applying the $n = 1$ external field. The advantage of using feedback is that the process adjusts itself to the most sensitive frequency, the effective external field pattern as well as its magnitude, compared with simply applying a predetermined perturbed field. The feedback used here was with a standard feedback hardware setup. The two sets of six feedback I-coils are located inside the vacuum vessel above and below the midplane. The connection of upper/lower coils was optimized for producing the $m/n = 3/1$ mode pattern. The feedback $n = 1$ signal was prepared using the poloidal magnetic field probes located at the midplane. More detail can be found in Ref. 26

Without feedback, the OFM activity showed the downward frequency chirping, forming a nearly steady-state $n = 1$ mode of $\sim$30 G as shown in the left column of Fig. 14. With feedback (right column), the coil current $\sim$500 A was requested and the measured magnetic perturbation amplitude was reduced to 10–15 G. Feedback did not completely suppress the mode. After the feedback process reduced the amplitude, the mode became a slowly rotating mode with frequency $\sim$500 Hz. Although the feedback was not successful, the reduction of amplitude indicates that the applied $n = 1$ field was well coupled to the mode, supporting the presence of the external kink character. The extremely low frequency and the sensitivity to external fields in the wall support that the mode at low frequency belongs to RWM.

The modest performance of feedback can be attributable to several factors. One possibility of this marginal performance is related to the nature of off-axis fishbone-driven RWM. As shown in Fig. 14, the initial mode frequency was too high so that the actuator power supply voltage was not sufficient enough to provide the requested current (inductive load limit). That is likely the reason why the coil current started with less than 100 A at the initial stage of feedback with above 5 kHz. Later, the coil current was increased to $\sim$500 A after the frequency was reduced to $\sim$1–2 kHz. The estimated peak magnetic field with 500 A coil currents is $\sim$7 G on the plasma surface, which is comparable to the mode amplitude. Thus, the feedback field is expected to vary the mode character. Another factor is the low gain. As observed, the mode became oscillatory with $\sim$500 Hz. This type of excitation with low-frequency oscillatory was attributable to the low gain operation with proportional gain as was observed in other current-driven-RWM experiments with low gain operation.[15,37]

VI. ANALYSIS WITH MARS-K

The rapid drop of EP losses and plasma rotation provides a unique approach for the assessment of the RWM kinetic stability. The experimental results of DIII-D RWM onset condition have been analyzed with the MARS-K code,[38] using both perturbative and self-consistent approaches.

The perturbative approach determines the growth rate with a first order approximation using the eigenfunction

Downloaded 04 Apr 2012 to 129.16.35.96. Redistribution subject to AIP license or copyright; see http://pop.aip.org/about/rights_and_permissions

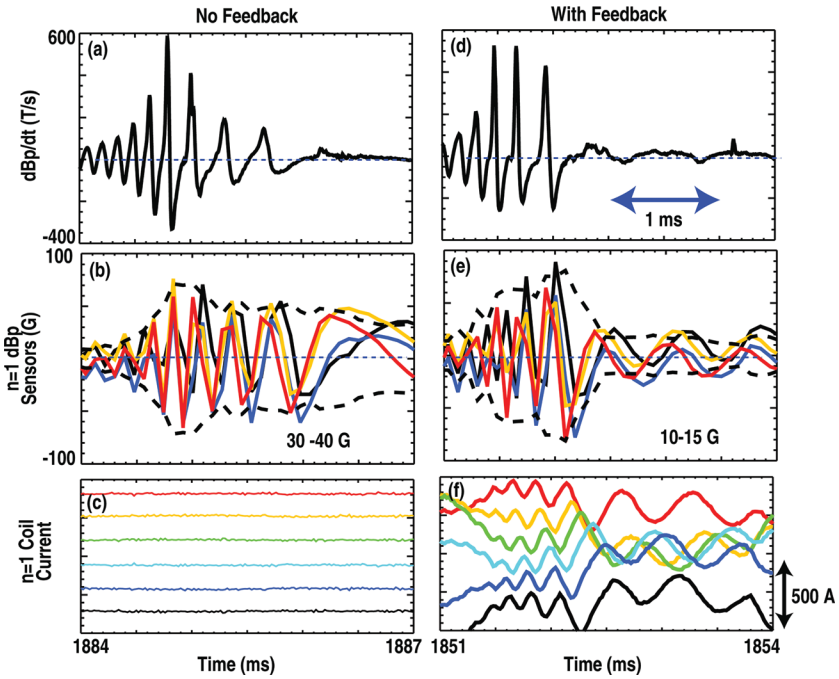

FIG. 14. (Color) Mode response to $n = 1$ additional field applied by the feedback without feedback #125638 (left) and with feedback #125639 (right) in DIII-D. (a) and (d) dBp/dt magnetic probe signal, (b) and (e) $n = 1$ δBp sensor signals at four different toroidal locations, and (c) and (f) feedback currents of six coils were shown with equal space vertical off-set for visibility. The scale of the coil current is illustrated at the right hand side.

from a linear ideal MHD stability code. Here, we use the eigenfunction computed with the MARS-K ideal-MHD option at zero rotation. The self-consistent approach is to find the eigenvalue and the eigenfunction without imposing any constraint on the eigenfunction. The kinetic contributions of both thermal (ions and electrons) and energetic ions are included by considering the precession drift resonances between the trapped particles and the mode. The equilibrium distribution function of the thermal particles is specified as Maxwellian, whereas the hot ions are specified by an isotropic (in particle pitch angle) slowing-down (in particle kinetic energy) distribution. This is a crude approximation for the beam energetic ions. A more detailed description of the MARS-K EP model is found in Ref. 39.

The equilibrium used in this analysis is reconstructed from the DIII-D shot #141069 at 1495 ms. The time traces for this shot are shown in Fig. 2 and the plasma parameters are listed in Table I. Figures 15(a)–15(d) show the equilibrium density, pressure, safety factor, and toroidal $E_r \times B_p$ rotation profiles. The reconstruction finds $q(0) = 1.55$ and $q_{95} = 4.60$.

In this calculation, observed rotation profile with CER is assumed to be same as the toroidal rotation profile. The normalized pressure β_N is 2.31, and the experimental central plasma rotation speed is about 4% of the toroidal Alfvén speed. The ideal-MHD computations using MARS-K, by scaling the plasma pressure, give a no-wall β_N limit of 2.14 and its ideal-wall limit of 2.60 (with the DIII-D wall shape). Thus, the RWM should be unstable for this DIII-D plasma, if no kinetic or rotational damping effects are taken into account.

Figure 15(e) shows the density and pressure profiles of the hot ions, normalized by the thermal density and pressure, respectively. In the plasma core, the hot ion density is about 10% of the total electron density, and the hot ion pressure is about 40% of the pressure for this DIII-D plasma. These hot ion profiles are computed from the experimental measurements and used as inputs to the MARS-K computations.

Figure 15(f) shows the radial profiles of the dominant poloidal harmonics of the normal displacement for the mode eigenfunction, in a PEST-like straight-field-line coordinate system. The mode has a large $m = 2$ component, in contrast

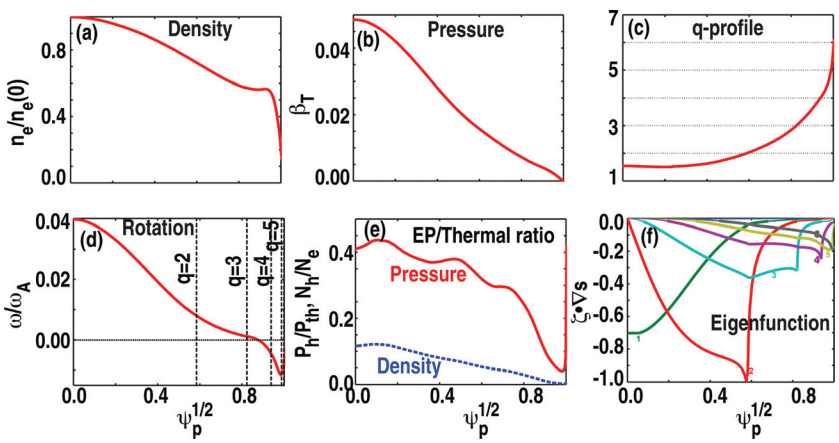

FIG. 15. (Color online) Equilibrium profiles vs. square root of poloidal flux in MARS-K analysis. (a) Density normalized to the central density, (b) plasma pressure shown by the plasma β_T, (c) q profile, (d) rotation frequency profile normalized to the central Alfvén rotation frequency, (e) the ratio of thermal component to EP, pressure (solid), density (dashed), and (f) poloidal component of eigenfunction with PEST-like coordinate.

Downloaded 04 Apr 2012 to 129.16.35.96. Redistribution subject to AIP license or copyright; see http://pop.aip.org/about/rights_and_permissions

to the classical fishbone mode that is dominated by $m = 1$ (Ref. 20). The eigenfunction generally has a global radial structure, with finite, but somewhat small displacement near the plasma edge. We also note that the $m = 3$ component is not small. This component is likely to contribute to the $m = 3$ mode pattern observed in these experiments.

We scale the plasma rotation amplitude from the experimental value down to zero, while fixing the shape of rotation profile to that shown in Fig. 15(d). We find that the perturbative approach predicts full stabilization of the RWM with the thermal particle contribution without hot ion kinetic contribution. Adding the hot ion kinetic contribution does not make a qualitative difference. In fact, hot ions only bring slight additional stabilization to the mode, at sufficiently fast plasma rotation. The strong drift kinetic stabilization of the mode, predicted by the perturbative approach, is due to the fact that the computed drift kinetic energy perturbation is much larger than the ideal MHD fluid energy perturbation. Much less stabilization is found by the self-consistent computations. Figure 16 shows the self-consistently computed stability boundary in a 2D plane, where we scale both the plasma central rotation amplitude, and a numerical parameter α_k, acting as a multiplier to the total perturbed kinetic energy

$$\delta W_k = \alpha_k \left(\delta W_{k,\mathrm{therm}} + \delta W_{k,\mathrm{EP}}\right). \tag{9}$$

Thus, $\alpha_k = 0$ means no kinetic contribution is included, and $\alpha_k = 1$ corresponds to full kinetic inclusion. Without the EP contribution, the thermal particles alone (dashed curve) cannot stabilize the RWM near the experimental condition before the off-axis fishbone event. With the inclusion of the EP contribution (solid curve), the RWM is predicted to be stable before the fishbone event. In fact the marginal boundary was reduced substantially by the hot ion contribution at higher plasma rotation. The stability boundary shown in Fig. 16 is rather complex. Qualitatively, this stability diagram can be explained as follows: with faster rotation, the EP precession can make a considerable contribution to δW_k, in particular for the imaginary part which comes from the particle–wave resonances. This is expected, since a better match of frequencies occurs between the EP precession drifts and the RWM rotation (in the plasma frame) with increasing ω_0.

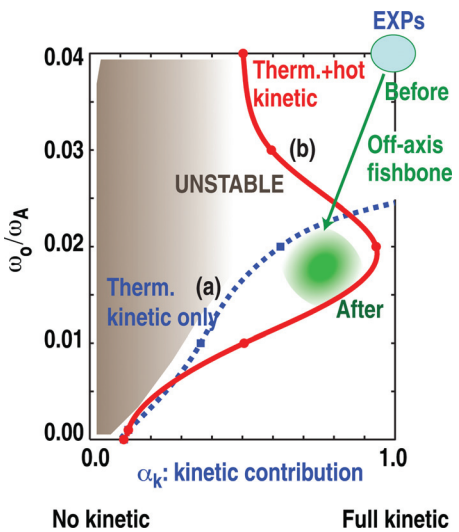

FIG. 16. (Color online) Marginal condition of plasma rotation and kinetic effect contribution (MARS-K analysis with self-consistent approach). The vertical axis is the central frequency normalized by the Alfvén frequency, $\omega(0)/\omega_A$ and the horizontal axis is the kinetic contribution factor [Eq. (9)] with (a) thermal kinetic only, and (b) thermal and EP kinetic effect included. A possible interpretation of OFM event is illustrated by the arrow; the transition from RWM stable to unstable state.

According to these results, the present experimental observations are interpreted in the following way: during the OFM burst, the plasma rotation drop of 10–15 km/s (more than 50%) from the initial rotation level and the EP losses ~10% leads to a less stable domain for the RWM from the initial experimental condition as indicated schematically in the figure. The self-consistent approach explains the experimental observation. The perturbative approach seems inadequate to describe the present results, overestimating the kinetic effects of thermal components.

VII. DISCUSSION AND SUMMARY

In both JT-60U and DIII-D devices, the EP-driven off-axis fishbone-like mode prevented long duration of high-β_N operation. This EP-driven mode was named as "energetic-particle-driven wall mode (EWM)" in the JT-60U and "off-axis-fishbone-driven" RWM in DIII-D. The observations in both devices have a strong commonality in the mode characteristics. In the following, we summarize separately the mode characteristics and the impact on the RWM stabilization. It is to be noted that since the neutron reduction and the rotation drop have not been clearly observed in these JT-60U experiments, the discussion related to the neutron and plasma rotation are based on the DIII-D results.

A. Off-axis-fishbone characteristics

All the characteristics of the OFM we have observed suggest the existence of a new EP-driven branch associated with the external kink, analogous to the EP-driven classical fishbone with the internal kink. First, the initial mode frequency and the frequency chirping phenomena lead to the conclusion that these modes can be categorized as EP precession-driven MHD modes. Second, the initial phase of OFM behaves just like a classical fishbone. We observed that the maximum neutron emission rate change vs. the maximum magnetic probe amplitude is similar to classical fishbone. Third, an external $n = 1$ field applied via feedback impacts the mode growth in DIII-D. This suggests that the mode has the external kink character when the frequency has chirped down to 1–2 kHz. Here, the external magnetic feedback served as an active tool for the mode identification. This suggests that it may be possible to suppress the RWM onset by impacting the transient process from the EP-driven mode to the RWM character, if the feedback system is improved.

A unique feature of OFM in contrast to the classical fishbone is nonlinear mode distortion as observed in both DIII-D and JT-60U. In DIII-D, the increase of EP loss rate observed by BILD coincided with the increase of the mode distortion. In JT-60U, the floating potential at the divertor target detecting the global SOL was increased up to ~100 V with sharp

Downloaded 04 Apr 2012 to 129.16.35.96. Redistribution subject to AIP license or copyright; see http://pop.aip.org/about/rights_and_permissions

positive spike with higher mode distortion, indicating EP losses. The mode distortion may have impacted the mode decay process. The evolution of the mode-decaying phase is far from the monotonic decay of a classical fishbone. It is to be noted that the plasma rotation drop is explainable with the EP loss-induced nonambipolar transport. Thus, the entire RWM stability process could be affected by the EP transport process.

One possible mode distortion in high beta plasmas was reported by Ref. 40 with $n = 1$ distortion in TFTR. As the high beta plasma reaches the ideal mode limit, a low n mode is first destabilized, and the plasma nonlinearly evolves as a 3D equilibrium containing a localized steep pressure gradient in the bad curvature region. This pressure gradient then can drive a new toroidally localized high-n mode, producing a local pressure bulge, which strongly pushes into the outer region of the plasma. In this case the mode distortion was localized on the steep pressure gradient. On the other hand, as observed in the OFM case, the mode distortion was extended over the entire mode structure as discussed in Sec. IV. Thus, the ballooning effect is unlikely for the OFM mode distortion. Further investigation of the entire time-evolution process of off-axis-fishbone-like mode is needed and will be useful to understand the EP stability and RWM suppression in future devices like ITER or DEMO, including alpha particles in burning plasmas.[39]

B. Impact on the RWM stabilization

During an OFM burst, the simultaneous reduction of EP density and the plasma rotation took place in DIII-D. The amounts of rotation reduction and EP losses are significant for the RWM stability in low rotation plasmas, which heavily relies on the kinetic effects, namely, on the EP density and the plasma rotation near the $q = 2$ surface. The rapid drop of both EP density and plasma rotation provides a unique approach for assessment of the RWM kinetic stability. The MARS-K analysis with self-consistent approach indicates that a possible reduction of the kinetic effect of the EP portion plays a dominant role in the experimental conditions and that the plasma rotation drop observed in the experiment can change the marginal stability limit significantly.

One interesting aspect is that the amount of rotation drop is consistent with the torque estimated to result from the radial drift of energetic ions as they are lost. The rotation drop can be considered as a byproduct of EP losses. Thus, the EP loss is a key parameter that governs the entire RWM stability in the low rotation regime.

There are several differences in DIII-D and JT-60U. In JT-60U, the RWMs are sometimes excited even with finite plasma rotation in contrast to near-zero rotation preference in DIII-D (Ref. 14). Furthermore, in JT-60U, EP-driven mode can also trigger ELMs that are synchronized with the EP-mode amplitude maximum.[17] At present, it is not clear whether these are significant differences or not. One possibility is that the anisotropy of EP distribution is much stronger in JT-60U due to the NBI geometry and the higher fast-ion density. Also, the EP-driven mode repetition frequency in JT-60U is quite different from in DIII-D, perhaps due to the fact that the explored β_N range in JT 60U is closer to the ideal-wall limit than in DIII-D or due to higher fast-ion pressure. Detailed analysis of JT-60U results with MARS-K is in preparation for resolving these issues.

Another interesting observation is the feedback performance. In this experiment, the feedback was an active tool to observe the impact of external magnetic fields on the mode, supporting the premise that the mode at near-zero frequency belongs to the RWM. The shift of mode behavior from near-steady to oscillatory behavior with feedback is attributable to the poor phase matching between the mode and the applied field. This indicates that the standard technique of phase adjustment in feedback logic could improve the feedback performance.

ACKNOWLEDGMENTS

This work was supported in part by the US Department of Energy under Contract Nos. DE-AC02-09CH11466, DE-FC02-04ER54698, SC-G903402, DE-FG02-08ER85195, and DE-FG02-04ER54761. This work was also supported by the U.S. Department of Energy (DOE) Fusion Energy Postdoctoral Research Program administered by the Oak Ridge Institute for Science and Education under DE-AC05-06OR23100. Additional support was provided by a Grant-in-Aid for Young Scientists (B) from the Ministry of Education, Culture, Sports, Science, and Technology of Japan, Grant No. 21760702.

The joint effort between JT-60U and DIII-D has been very productive in identifying the mode. In particular, the nonlinear process of mode distortion would have been hard to evaluate, if the investigation had been limited only to one device.

We are very grateful for JAEA and GA organizations for their encouragement to pursue this subject as a joint undertaking. We are also thankful to Dr. N. Gorelenkov and Dr. G. Fu who provided several suggestions regarding classical fishbone and mode distortion. We also express thanks to Dr. R. Nazikian who encouraged us to pursue the experiment of the off-axis-fishbone-driven RWM in DIII-D.

[1]A. D. Turnbull, T. S. Taylor, Y.R. Lin-Liu, and H. St. John, Phys. Rev. Lett. **74**, 718 (1995).
[2]J. P. Freidberg, *Ideal Magnetohydrodynamics* (Plenum, New York, 1987), p.309.
[3]A. Bondeson and D. J. Ward, Phys. Rev. Lett. **72**, 2709 (1994).
[4]M. S. Chu and M. Okabayashi, Plasma Phys. Controlled Fusion **52**, 123001 (2010).
[5]M. Takechi, G. Matsunaga, N. Aiba, T. Fujita, T. Ozeki, Y. Koide, Y. Sakamoto, G. Kurita, A. Isayama, Y. Kamada, and the JT-60 Team, Phys. Rev. Lett. **98**, 055002 (2007).
[6]G. Matsunaga, M. Takechi, N. Aiba, G. Kurita, Y. Sakamoto, Y. Koide, A. Isayama, T. Suzuki, T. Fujita, N. Oyama, T. Ozeki, Y. Kamada, and JT-60 Team, Plasma Fusion Res. **4**, 051 (2009).
[7]H. Reimerdes, A. M. Garofalo, G. L. Jackson, M. Okabayashi, E. J. Strait, M. S. Chu, Y. In, R. J. La Haye, M. J. Lanctot, Y. Q. Liu, G. A. Navratil, W. M. Solomon, H. Takahashi, and R. J. Groeber, Phys. Rev. Lett. **98**, 055001 (2007).
[8]E. J. Strait, A. M. Garofalo, G. L. Jackson, M. Okabayashi, H. Reimerdes, M. S. Chu, R. Fitzpatrick, R. J. Groebner, Y. In, R. J. La Haye, M. J. Lanctot, Y. Q. Liu, G. A. Navratil, W. M. Solomon, and H. Takahashi, Phys. Plasmas **14**, 056101 (2007).
[9]A. Bondeson and M. S. Chu, Phys. Plasmas **3**, 3013 (1996).
[10]B. Hu, R. Betti, and J. Manickam, Phys. Plasmas **12**, 057301 (2005).
[11]Y. Q. Liu, M. S. Chu, I. T. Chapman and T. C. Hender, Nucl. Fusion **49**, 035004 (2009).

Downloaded 04 Apr 2012 to 129.16.35.96. Redistribution subject to AIP license or copyright; see http://pop.aip.org/about/rights_and_permissions

[12]H. Reimerdes, A. M. Garofalo, E. J. Strait, R. J. Buttery, M. S. Chu, Y. In, G. L. Jackson, R. J. La Haye, M. J. Lanctot, Y. Q. Liu, M. Okabayashi, J.-K. Park, M. J. Schaffer, and W. M. Solomon, Nucl. Fusion **49**, 115001 (2009).
[13]J. W. Berkery, S. A. Sabbagh, H. Reimerdes, R. Betti, B. Hu, R. E. Bell, S. P. Gerhardt, J. Manickam, and M. Podestà, Phys. Plasmas **17**, 082504 (2010).
[14]G. Matsunaga, N. Alba, K. Shinohara, Y. Sakamoto, A. Isayama, M. Takechi, T. Suuki, N. Oyama, N. Asakura, Y. Kamada, and T. Ozeki, Phys. Rev. Lett. **103**, 045001 (2009).
[15]M. Okabayashi, I. N. Bogatu, M. S. Chance, M. S. Chu, A. M. Garofalo, Y. In, G. L. Jackson, R. J. La Haye, M. J. Lanctot, J. Manickam, L. Marrelli, P. Martin, G. A. Navratil, H. Reimerdes, E. J. Strait, H. Takahashi, A. S. Welander, T. Bolzonella, R. V. Budny, J. S. Kim, R. Hatcher, Y. Q. Liu, and T. C. Luce, Nucl. Fusion **49**, 125003 (2009).
[16]G. Matsunaga, K. Shinohara, N. Aiba, Y. Sakamoto, A. Isayama, N. Asakura, T. Suzuki, M. Takechi, N. Oyama, H. Urano, and the JT-60 Team, Nucl. Fusion **50**, 084003 (2010).
[17]G. Matsunaga, N. Aiba, K. Shinohara, Y. Sakamoto, M. Takechi, T. Suzuki, N. Asakura, A. Isayama, N. Oyama, M. Yoshida, K. Kamiya, H. Urano, T. Nakano, Y. Kamada, and the JT-60 Team, in Proceedings of 23rd IAEA Fusion Energy Conference, Daejeon, Republic of Korea (2010). Available at http://www-pub.iaea.org/mtcd/meetings/cn180_papers.asp, Paper EXS/5-3.
[18]K. McGuire, R. Goldston, M. Bell, M. Bitter, K. Bol, K. Brau, D. Buchenauer, T. Crowley, S. Davis, F. Dylla, H. Eubank, H. Fishman, R. Fonck, B. Grek, R. Grimm, R. Hawryluk, H. Hsuan, R. Hulse, R. Izzo, R. Kaita, S. Kaye, H. Kugel, D. Johnson, J. Manickam, D. Manos, D. Mansfield, E. Mazzucato, R. McCann, D. McCune, D. Monticello, R. Motley, D. Mueller, K. Oasa, M. Okabayashi, K. Owens, W. Park, M. Reusch, N. Sauthoff, G. Schmidt, S. Sesnic, J. Strachan, C. Surko, R. Slusher, H. Takahashi, F. Tenney, P. Thomas, H. Towner, J. Valley, and R. White, Phys. Rev. Lett. **50**, 891 (1983).
[19]F. Porcelli, Plasma Phys. Controlled Fusion **33**, 1601 (1991).
[20]C. Cheng, Phys. Rep. **211**(1), 1 (1992).
[21]D. J. Campbell, D. F. H. Start, J. A. Wessen, D. V. Barlett, V. P. Bhatnagar, M. Bures, J. G. Cordey, G. A. Cottrell, P. A. Dupperex, A. W. Edwards, C. D. Challis, C. Gormezano, C. W. Gowers, R. S. Granets, J. H. Hamnen, T. Hellsten, J. Jacquinot, E. Lazarro, P. J. Lomas, N. Lopes Cardozo, P. Mantica, J. A. Snipes, D. Stork, P. E. Stott, P. R. Thomas, E. Thompson, K. Thomsen, and G. Tonetti, in Proceedings of 11th International Conference on Plasma Physics and Controlled Nuclear Fusion, Kyoto, Japan, Vol. 1 (IAEA, Vienna, 1987).
[22]S. Tokuda and T. Watanabe, Phys. Plasmas **6**, 3012 (1999).
[23]L. C. Bernard, F. J. Helton, and R. W. Moore, Comput. Phys. Commun. **24**, 377 (1981).
[24]A. Glasser and M. S. Chance, Bull. Am. Phys. Soc. **42**, 1848 (1997).
[25]J. Bialek, A. Boozer, M. Mauel, and G. Navratil, Phys. Plasmas **8**, 2170 (2001).
[26]M. Okabayashi, J. Bialek, A. Bondeson, M. S. Chance, M. S. Chu, A. M. Garofalo, R. Hatcher, Y. In, G. L. Jackson, R. J. Jayakumar, T. H. Jensen,O. Katsuro-Hopkins, R. J. La Haye, Y. Q. Liu, G. A. Navratil, H. Reimerdes, J. T. Scoville, E. J. Strait, M. Takechi, A. D. Turnbull, P. Gohil, J. S. Kim, M. A. Makowski, J. Manickam, and J. Menard, Nucl. Fusion **45**, 1715 (2005).
[27]K. Shinohara, S. Sakurai, M. Ishikawa, K. Tsuzuki, Y. Suzuki, K. Masaki, O. Naito, K. Kurihara, T. Suzuki, Y. Koide, T. Fujita, Y. Miura, and the JT-60 Team, Nucl. Fusion **47**, 997 (2007).
[28]W. W. Heidbrink and G. Sadler, Nucl. Fusion **34**, 535 (1994).
[29]W. W. Heidbrink, Phys. Plasmas **15**, 055501 (2008).
[30]R. White, R. J. Goldson, K. McGuire, A. H. Boozer, D. A. Monticello, and W. Park, Phys. Fluids **26**, 2958 (1983).
[31]J. S. deGrassie, J. E. Rice, K. H. Burrell, R. J. Groebner, and W. M. Solomon, Phys. Plasmas **14**, 057115 (2007).
[32]Y. B. Zhu, W. W. Heidrink, and L. D. Pickering, Nucl. Fusion **50**, 084024 (2010).
[33]R. K. Fisher, D. C. Pace, M. García-Muñoz, W. W. Heidbrink, C. M. Muscatello, M.A. Van Zeeland, and Y. B. Zhu, Rev. Sci. Instrum. **81**, 10D307 (2010).
[34]G. W. Watson, and W. W. Heidbrink, Rev. Sci. Instrum. **74**, 1605 (2003).
[35]J. G. Watkins, J. Salmonson, R. Moyer, R. Doemer, R. Lehmer, L. Schmitz, and D. N. Hill, Rev. Sci. Instrum. **63**, 4728 (1992).
[36]W. W. Heidbrink, M. E. Austin, R. K. Fisher, M. Garcia-Munoz, G. Matsunaga, G. R. McKee, R. A. Moyer, C. M. Muscatello, M. Okabayashi, D. C. Pace, K. Shinohara, W. M. Solomon, E. J. Strait, M.A. Van Zeeland, and Y. B. Zhu, "Characterization of off-axis fishbones," Phys. Plasmas Controlled Fusion (submitted).
[37]Y. In, M. S. Chu, G. L. Jackson, J. S. Kim, R. J. La Haye, Y. Q. Liu, L Marrelli, M. Okabayashi, H. Reimerdes, and E. J. Strait, Plasma Phys. Controlled Fusion **52**, 104004 (2010).
[38]Y. Liu, M. S. Chu, W. F. Guo, F. Villone, R. Albanese, G. Ambrosino, M. Baruzzo, T. Bolzonella, I. T. Chapman, A. M. Garofalo, C. G. Gimblett, R. J. Hastie, T. C. Hender, G. L. Jackson, R. J. La Haye, M. J. Lanctot, Y. In, G. Marchiori, M. Okabayashi, R. Paccagnella, M. Furno Palumbo, A. Pironti, H. Reimerdes, G. Rubinacci, A. Soppelsa, E. J. Strait, S. Ventre, and D. Yadykin, Plasma Phys. Controlled Fusion **52**, 104002 (2010).
[39]Y. Liu, Nucl. Fusion **50**, 095008 (2010).
[40]W. Park, E. Fredrickson, A. Janos, J. Manickam, and W. Tang, Phys. Rev. Lett. **72**, 1763 (1995).

Downloaded 04 Apr 2012 to 129.16.35.96. Redistribution subject to AIP license or copyright; see http://pop.aip.org/about/rights_and_permissions